AGU PUBLICATIONS

Geochemistry, Geophysics, Geosystems

RESEARCH ARTICLE
10.1002/2014GC005307

**Key Points:**
- The 3-D aseismic slip distribution on the Ismetpasa segment revealed by modeling
- Creeping section considerably longer than those estimated by previous studies
- Fault creep can be correlated with geology at shallow depths along the NAF

**Supporting Information:**
- Readme
- Figures S1–S4

**Correspondence to:**
E. Cetin,
esra.cetin@itu.edu.tr

**Citation:**
Cetin, E., Z. Cakir, M. Meghraoui, S. Ergintav, and A. M. Akoglu (2014), Extent and distribution of aseismic slip on the Ismetpaşa segment of the North Anatolian Fault (Turkey) from Persistent Scatterer InSAR, *Geochem. Geophys. Geosyst.*, *15*, doi:10.1002/2014GC005307.

Received 20 FEB 2014
Accepted 23 JUN 2014
Accepted article online 25 JUN 2014

# Extent and distribution of aseismic slip on the Ismetpaşa segment of the North Anatolian Fault (Turkey) from Persistent Scatterer InSAR

**Esra Cetin[1,2], Ziyadin Cakir[1], Mustapha Meghraoui[2], Semih Ergintav[3], and Ahmet M. Akoglu[4]**

[1]Department of Geology, Istanbul Technical University, Istanbul, Turkey, [2]EOST-UMR 7516, Institut de Physique du Globe de Strasbourg, Strasbourg, France, [3]Department of Geodesy, Kandilli Observatory and Earthquake Research Institute, Bogaziçi University, Istanbul, Turkey, [4]Division of Physical Sciences and Engineering, King Abdullah University of Science and Technology, Thuwal, Saudi Arabia

**Abstract** We use the Persistent Scatterer InSAR (PSI) technique with elastic dislocation models and geology along the creeping section of the North Anatolian Fault (NAF) at Ismetpaşa, to map and deduce the velocity field and the aseismic slip distribution. Revealing the spatiotemporal nature of the creep helped us associate the creep with potential lithological controls, hence providing a new perspective to better understand the underlying causes and mechanisms. The PSI analysis of Envisat ASAR images between 2003 and 2010 reveals a clear picture of surface creep along the fault and a new interseismic velocity field transitioning gradually between the creeping and the locked fault sections. The creep rate is found to fluctuate along a 100 km long section of the fault in a manner similar to that along the Hayward fault, reaching a maximum of $\sim 20 \pm 2$ mm/yr, close to the far field plate velocity ($\sim 25 \pm 1.5$ mm/yr). At Ismetpaşa, it is in the range of $8 \pm 2$ mm/yr, consistent with the previous geodetic observations. The creeping section appears to extend 30 km further east than those previously reported. Modeling of the PSI data reveals a heterogeneous creep distribution at depth with two main patches confined mostly to the uppermost 5 km portion of the seismogenic crust, releasing annually $6.2 \times 10^{16}$ Nm (Mw = 5.1) geodetic moment. Our analysis combined with previous studies suggests that creep might have commenced as postseismic deformation following the 1944 earthquake and has evolved to stable fault creep with time. There is a correlation between aseismic surface creep and the geology along the fault as it is in major part associated to rocks with low frictional strength such as the andesitic-basaltic, limestone, and serpentine bodies within the fault zone.

## 1. Introduction

Understanding the mechanics of major active faults is important for reliable seismic hazard evaluations and better understanding of the earthquake physics [*Carpenter et al.*, 2011]. Although the majority of active faults may be locked, accumulating strain over a long period of time (e.g., up to 300 years along a single segment of the North Anatolian Fault [*Barka*, 1996]) and releasing it abruptly during moderate-to-large earthquakes (Mw > 6), some faults slip freely, accumulating little or no strain and generating no significant earthquakes [*Thatcher*, 1979; *Burford and Harsh*, 1980]. Faults that exhibit surface creep can appear to be locked at shallow or midcrustal depths, but nevertheless episodically produce moderate earthquakes. Examples of such partially locked faults include the Hayward fault [*Savage and Lisowski*, 1993; *Schmidt et al.*, 2005], the Superstition Hills fault [*Bilham*, 1989; *Wei et al.*, 2009], the Longitudinal Valley fault [*Champenois et al.*, 2012; *Thomas et al.*, 2014], and the Ismetpaşa segment of the North Anatolian Fault [*Ambraseys*, 1970; *Cakir et al.*, 2005]. Knowledge of the extent and rate of aseismic creep on the fault plane is therefore critical for reliable assessment of seismic hazard as it effectively reduces the fault surface area capable of rupture in earthquakes. Its spatiotemporal variation along faults has also important implications for forecasting the timing, locations, and potential sizes of future earthquakes and for understanding the fault behavior [*Bürgmann et al.*, 2000].

The Ismetpaşa creeping segment was ruptured by the 1944 Bolu-Gerede (M = 7.3) and 1951 Kurşunlu (M = 6.9) earthquakes, part of the westward migrating earthquake sequence of the NAF during the twentieth century (Figure 1) [*Barka and Kadinsky-Cade*, 1988; *Barka*, 1996; *Stein et al.*, 1997]. Based on the railway maintenance reports, *Ambraseys* [1970] estimated a rapid right-lateral surface creep of 50 mm/yr following

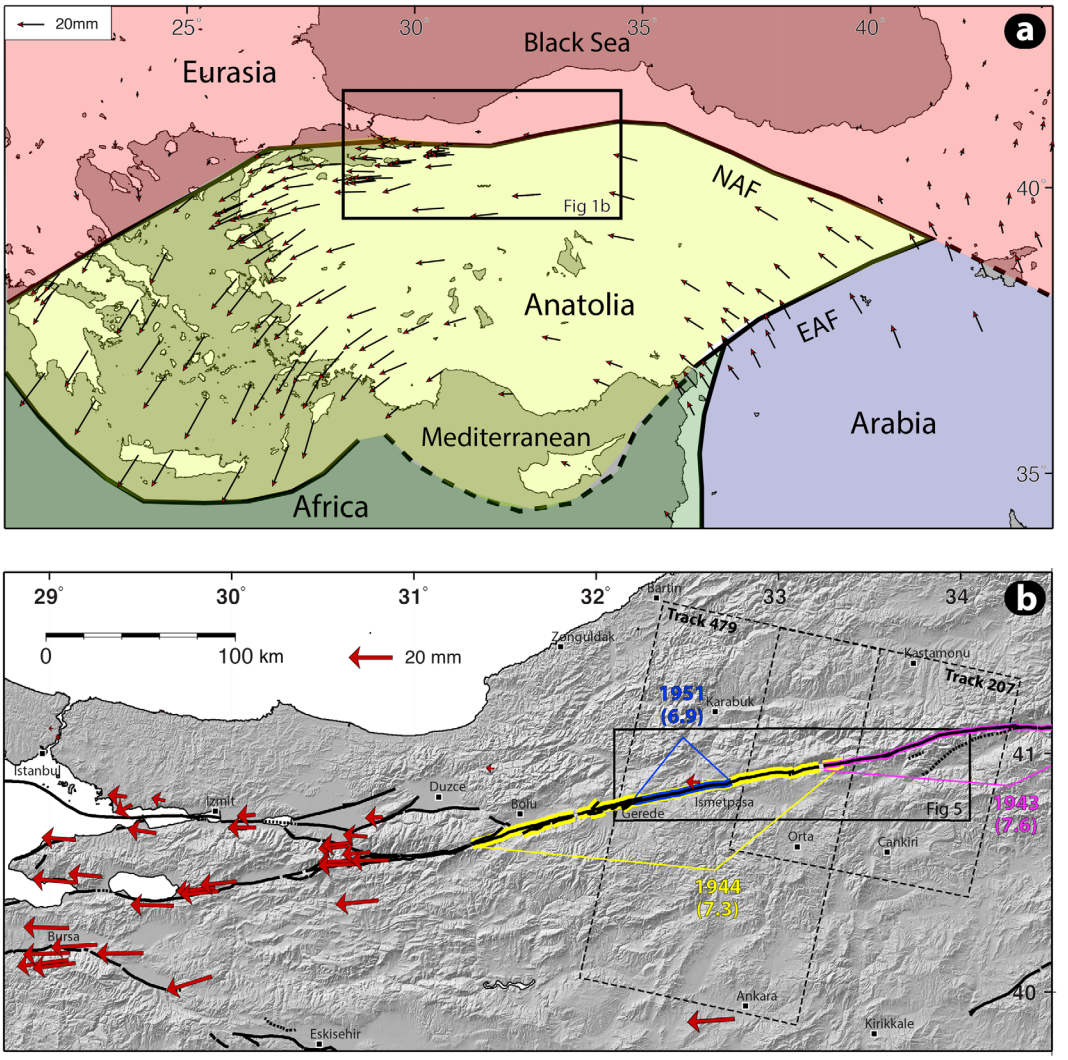


**Figure 1.** (a) Tectonic map of Turkey and surrounding regions with GPS vectors in a Eurasia fixed reference frame [*Reilinger et al*., 2006]. Rectangle shows the location of Figure 1b. (b) Shaded SRTM topography map along the North Anatolian Fault zone in northwestern Turkey with the recent rupture segments of large earthquakes [*Barka and Kadinsky-Cade*, 1988; *Şaroğlu et al*., 1992]. The dashed rectangles are the Envisat image frames with track numbers used in this study.

the 1944 earthquake until the 1951 event. The spatiotemporal evolution of the surface creep at Ismetpaşa remained, however, unknown until the mid-2000s despite its discovery in the late sixties [*Ambraseys*, 1970]. Offset measurements on the walls of the railway station at Ismetpaşa town suggested that the creep rate had decreased to 20 mm/yr between 1957 and 1969 [*Ambraseys*, 1970]. A microgeodetic network installed across the fault at Ismetpaşa in 1972, added with other geodetic measurements (LIDAR and InSAR) along the creeping segment, shows an exponential or logarithmic decrease of creep rate reaching a steady slip rate of about 9 mm/yr over the last decade [*Aytun*, 1982; *Eren*, 1984; *Deniz et al*., 1993; *Cakir et al*., 2005; *Kutoglu and Akcin*, 2006; *Kutoglu et al*., 2008; *Kutoglu et al*., 2010; *Karabacak et al*., 2011; *Ozener et al*., 2012; *Kaneko et al*., 2013]. Using the conventional InSAR method, *Cakir et al*. [2005] identified, for the first time, a 70 km long lateral extent of the creeping section, roughly confirmed later on by *Kaneko et al*. [2013] using stacking of independent InSAR data.

In this study we present an interseismic velocity field mapped using the Persistent Scatterer InSAR (PSI) time series technique [*Ferretti et al*., 2001; *Hooper et al*., 2004] between 2003 and 2010 on two overlapping descending tracks of Envisat ASAR (C-band) satellite covering the NAF between 32.1°E and 34.3°E (Figure 1). We use the surface velocity field and provide for the first time a model of aseismic slip distribution on the fault using elastic half-space dislocations. Finally, we discuss the mechanism of aseismic creep, its

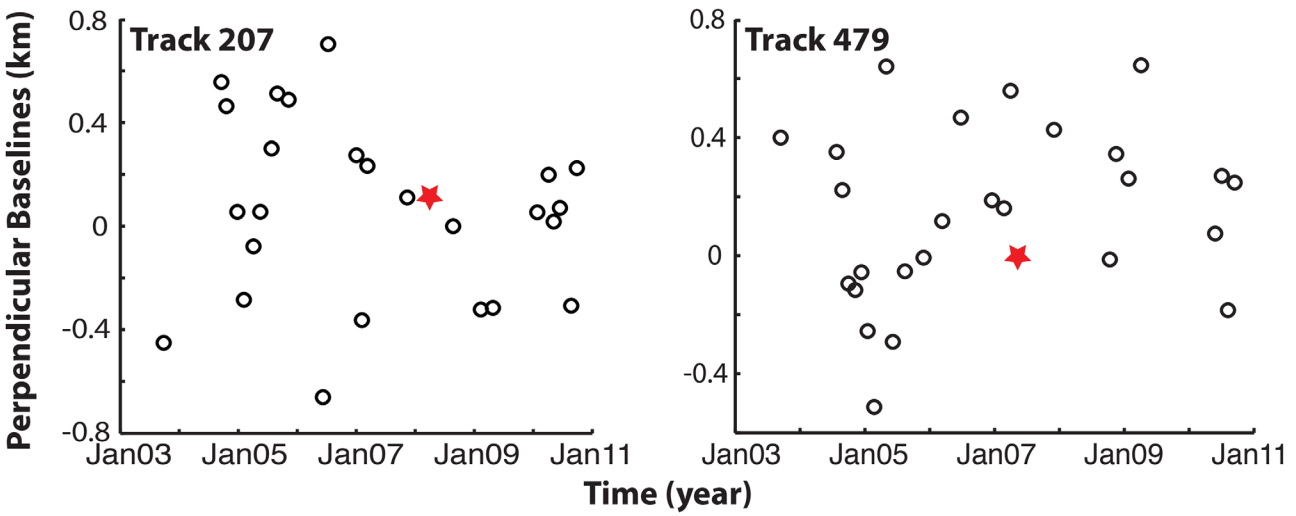


**Figure 2.** Baseline versus time plot of synthetic aperture radar orbits from two Envisat tracks used to calculate the deformation field and the time series. Empty circles denote the SAR images with stars indicating the master orbits chosen for the PSI analyses.

initiation, and the potential causes for its along-strike variation on the basis of creep rate variation and lithology along the fault.

## 2. InSAR Observations

The PSI method is an advanced multitemporal InSAR technique, capable of simultaneous processing of multiple SAR acquisitions in time, which will increase the number of locations where a subtle deformation signal can be extracted by reducing the associated errors [*Ferretti et al*., 2001]. It has been successfully used to reveal slow surface creep along the Longitudinal Valley (Eastern Taiwan) [*Champenois et al*., 2012] and Izmit (Turkey) faults [*Cakir et al*., 2012]. Such advanced techniques are able to reduce the effects of noise and signal decorrelation due to atmospheric effects, digital elevation model (DEM) errors, and orbital inaccuracies [*Hooper*, 2008]. Compared to conventional InSAR, the PSI analysis generates time series of ground deformations for individual targets using multitemporal stacks of synthetic aperture radar (SAR) images with regard to these targets that have a constant echo over the time are called persistent scatterers (PS) [*Ferretti et al*., 2000; *Hooper et al*., 2004; *Kampes*, 2005; *Motagh et al*., 2007; *Cigna et al*., 2011; *Peyret et al*., 2011; *Dehghani et al*., 2013]. There are various PSI approaches to detect the PS pixels and estimate the ground deformation signal [*Ferretti et al*., 2001; *Hooper et al*., 2007; *Ketelaar*, 2008]. In comparison, PS selection algorithms and deformation estimation methods are different in between these approaches. In this study, we present interseismic velocity fields obtained from PSI analysis with a single master network using the StaMPS (Stanford Method for PS) software package that takes the advantage of spatial correlation between pixels and does not use any temporal deformation model in the PS identification step [*Hooper*, 2008; *Dehghani et al*., 2013]. The PS pixels are successfully detected through the phase analysis in a series of iterations even though their amplitude is low. The StaMPS uses ROI_PAC software [*Rosen et al*., 2004] for focusing the raw images and DORIS software [*Kampes and Usai*, 1999] for calculating interferograms with the SRTM 90 m DEM data [*Farr et al*., 2007] for removal of the topographic phase contribution. Orbital errors are estimated and removed from the mean line-of-sight (LOS) velocity field with a best fit bilinear ramp. Potential unwrapping errors in each interferogram were checked visually as recommended by *Hooper* [2008]. Velocity standard deviation maps, calculated by StaMPS using bootstrapping, reach a maximum of 2.4 mm/yr for two individual overlapping tracks (Figure S1, supporting information). The detailed processing procedure can be found in *Hooper* [2008].

### 2.1. Surface Velocity Field

We have analyzed 55 Envisat ASAR images on two descending and overlapping tracks (T479 and T207; Figure 1b) between 2003 and 2010 (Figure 2). Images acquired on 6 May 2007 on T479 and 8 August

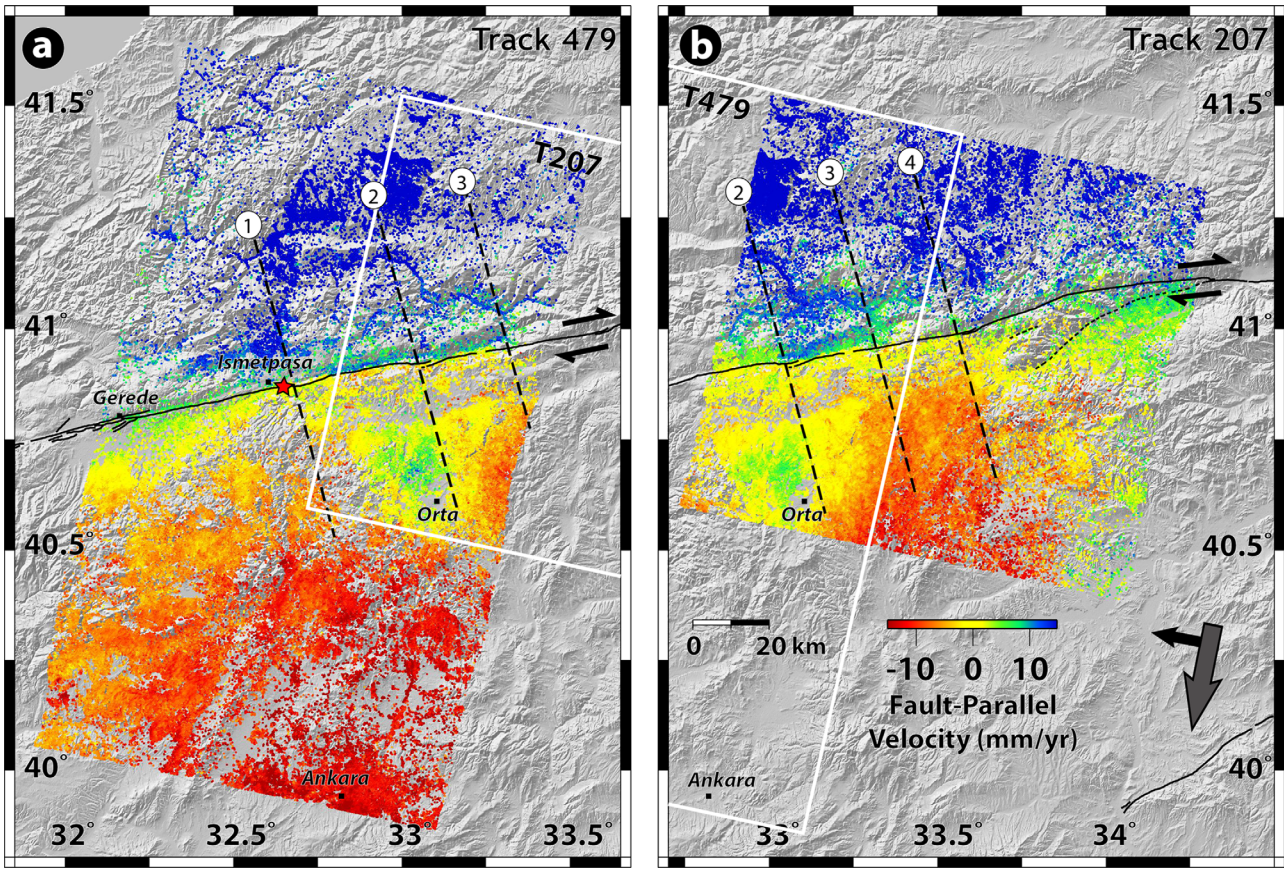


**Figure 3.** Velocity field in the region of Ismetpaşa deduced from PSI time series. (a, b) Fault-parallel horizontal velocity field (identical color scale for both tracks) between 2003 and 2010 on a SRTM shaded relief image with known active faults (black lines). The gray and black arrows to the bottom right corner show the satellite flight direction (descending) and the line-of-sight direction (right looking), respectively. Movements away from the satellite are shown with warm colors and toward the satellite are shown with cool colors, which are consistent with the right-lateral sense of motion of the NAF. Thick dashed lines with numbers are locations of profiles as shown in Figure 4. Red star shows the location of the PSI and GPS time series plotted in Figure 7. White boxes show the neighboring Envisat track used in this study.

2008 on T207 are chosen as the master scenes of all the interferometric pairs in each track to minimize the spatial and temporal decorrelation and atmospheric effects. A mean radar line-of-sight (LOS) velocity field for each track is obtained and then projected to fault-parallel horizontal velocities assuming that the radar LOS displacements are due to purely horizontal motion on a N76°E trending strike-slip fault, parallel to the strike of the Ismetpaşa segment taking into account the local incidence angles that vary across the range. The fault-parallel velocity field shown in Figure 3 reveals very clearly the surface creep as well as the interseismic strain accumulation across the NAF. Warm colors (i.e., negative velocities) on the southern side of the fault indicate motion away from the satellite (i.e., westward) and cool colors (i.e., positive velocities) on the northern side of the fault indicate motion toward the satellite (i.e., eastward), consistent with a right-lateral sense of plate motion across the NAF. Surface creep is characterized by steep fault-parallel velocity gradients and by a sharp color contrast across the fault trace along a distance of more than 100 km (Figure 3). In contrast, locked segments are clearly shown by gradual changes in the velocity field across the fault, particularly between Gerede and Ismetpaşa. Besides, to the south of the NAF the interseismic signal is strongly disturbed by a circular deformation pattern attributed to the postseismic displacements after the 6 June 2000 Orta earthquake [*Taymaz et al*., 2007; *Cakir and Akoglu*, 2008].

Fault-parallel velocities along four different profiles are shown in Figure 4 together with best fit models for creeping and locked faults obtained with elastic dislocations. The velocity profiles of locked faults (at 15 km depth) show a classic arctangent shape predicted by elastic screw dislocations across a strike-slip fault [*Savage and Burford*, 1973]. Conversely, the steps in the velocity profiles at the fault indicate surface creep. The shape and height of these steps are controlled by the locking depth and creep rate; abrupt vertical changes

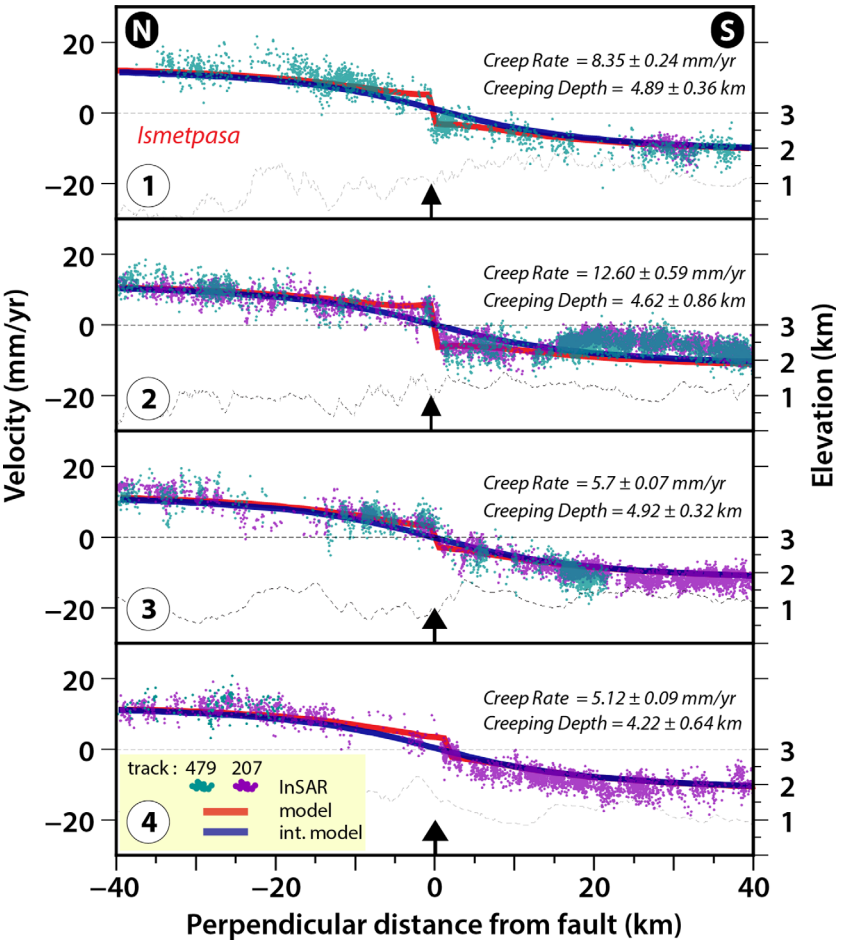


**Figure 4.** Observed and modeled fault-parallel velocity profiles perpendicular to the fault. Red curves show the best fitting model to PSI data with the creep rate and depth given above. The blue curves represent an interseismic model for a locked fault at 15 km of depth. Dashed line represents the topographic elevation along the profiles. Arrows indicate the mapped active fault location. Profile-1 crosses the location of the offset wall and the geodetic network that have been used to measure the creep rate at Ismetpaşa over the last 40 years.

indicating creep reaching to the surface, and gradual changes showing deeper locking depths. It is worthwhile noting that fault-parallel velocities in Figure 4 do not correlate with topography.

### 2.2. Estimation of Creep Rate and Extent

In order to determine the surface creep rate and its variations along the fault, we first subtract from the velocity field the interseismic model as explained in the modeling section below. Subsequently, profiles of residual velocities perpendicular to the fault are extracted at every ~1 km along the fault. Along 3 km on each side of the fault, we find a best fitting line to the profiles and compute the creep rate as an offset of the intercepts of these two lines at the fault trace (Figure 5) [*Burford and Harsh*, 1980]. Using standard

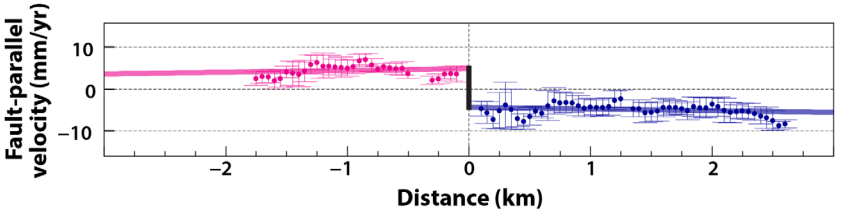


**Figure 5.** Estimation procedure for the creep rate using best fitting lines to InSAR velocity profiles that extend for 3 km on both sides of the fault (pink and blue colors). Creep rate is calculated from the offset of the two lines at the fault trace (e.g., the length of black line).

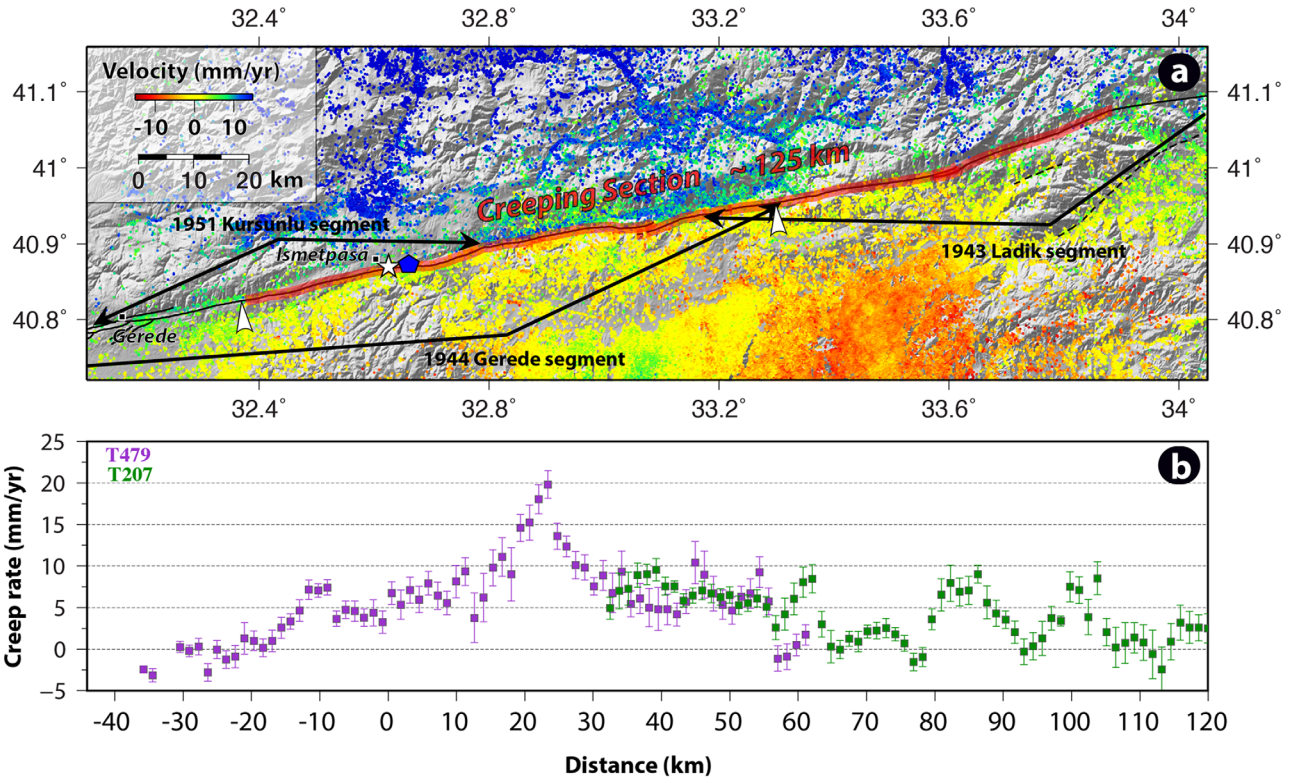


**Figure 6.** Rate and extent of aseismic surface creep along the Ismetpaşa section of the North Anatolian Fault. (a) A mosaicked map of fault-parallel horizontal velocity field on SAR image tracks T479 and T207. Red line shows the creeping section of the NAF and the blue pentagon indicates the location of the micro-GPS network. White star represents the location of the wall where creep was discovered by *Ambraseys* [1970]. White arrows show the extents previously found by *Cakir et al.* [2005] and *Kaneko et al.* [2013]. (b) Creep rates with error bars along the fault are estimated from the InSAR velocities on track T479 (pink color) and track T207 (green color).

deviations of PS pixels predicted by StaMPS, weighted means are calculated at every 50 m using a bin width of 100 m along these fault perpendicular profiles. The error bars of creep rates for individual profiles are estimated from the root-mean-square residuals of the curve fitting using weighted means. The results reveal a ∼120 km long creeping section with a creep rate varying in an oscillating manner along the fault and reaching a maximum of 20 ± 2 mm/yr around 20 km east of Ismetpaşa (Figure 6). At its eastern end, it overlaps with the western part of the 1943, and the eastern part of the 1944 and 1951 earthquake ruptures (Figure 6a). Note that despite some discrepancies, creep rate estimates from two different InSAR data sets

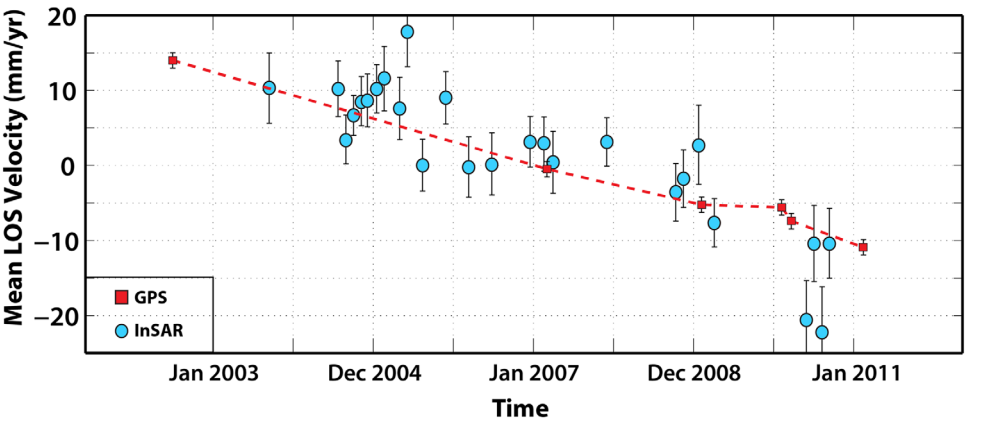


**Figure 7.** Time series of line-of-sight InSAR (blue circles) and GPS (red squares) velocities (blue pentagon shown in Figure 6) [*Ozener et al.*, 2012]. The LOS velocities represent the mean of all pixels in a circle of ∼600 m diameter to the north and south of the fault around the GPS network. The general trend and decay of creeping rate from InSAR time series are in good agreement with GPS time series.

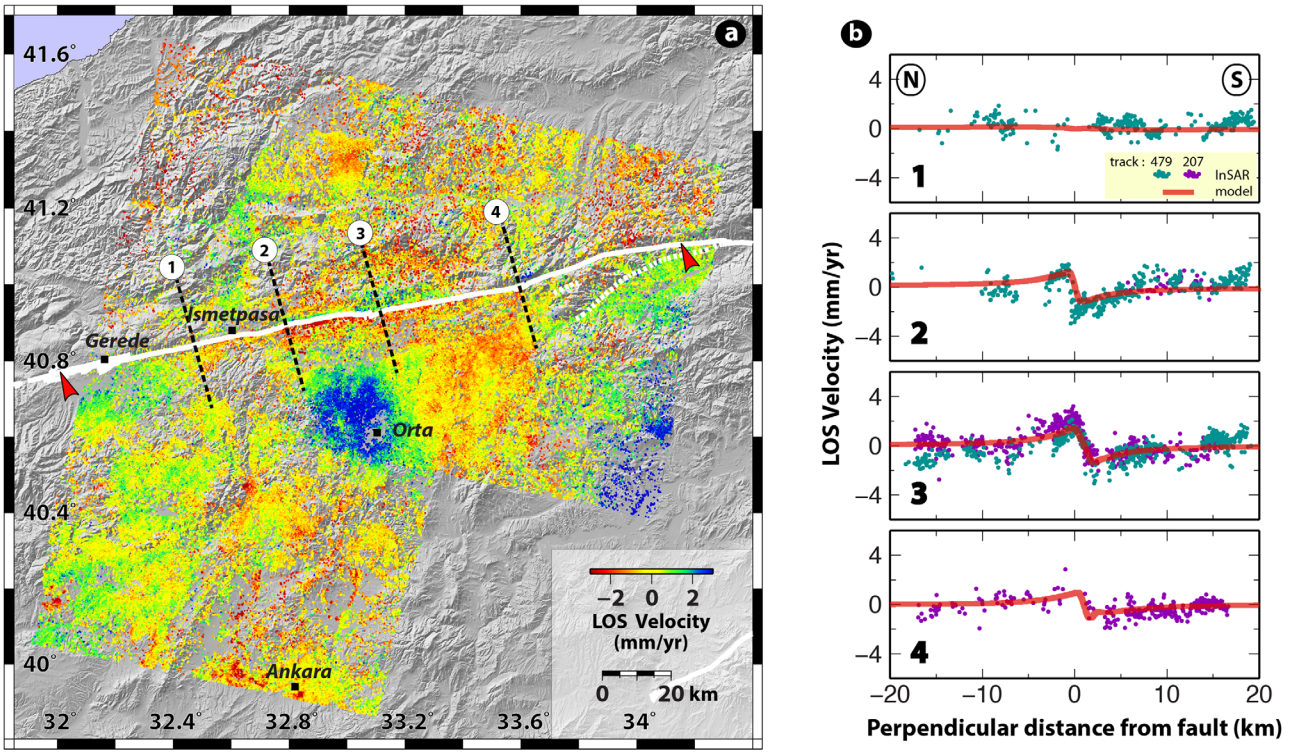


**Figure 8.** Modeling of aseismic slip distribution. (a) Residual LOS velocities, obtained by the removal of the long-term signal due to interseismic loading and unwrapping, atmospheric, and orbital errors, are used to model the aseismic slip on the fault. The blue circular anomaly located around the town of Orta is most likely due to the postseismic deformation of the 6 June 2000 Orta earthquake (Mw = 6.0). Red arrows on the fault (white lines) indicate the tips of the modeled fault shown in Figure 9. Dashed lines show the profiles in Figure 8b. (b) Observed (green and purple points) and modeled residual velocities (red lines) along the profiles perpendicular to the fault.

in the central section of the fault are overall in good agreement. The creep rate is 8 ± 2 mm/yr at Ismetpaşa, consistent with most previous studies [*Deniz et al*., 1993; *Cakir et al*., 2005; *Karabacak et al*., 2011; *Ozener et al*., 2012; *Kaneko et al*., 2013]. The InSAR LOS time series are in good agreement with LOS-projected GPS time series at Ismetpaşa [*Ozener et al*., 2012] and show linear decays with time (Figure 7).

## 3. Modeling

To estimate the aseismic slip distribution on the Ismetpaşa segment, we model the LOS displacements using the Poly3Dinv software [*Maerten et al*., 2005] that uses the boundary element approach. To infer the aseismic slip distribution on the fault, we first model and remove from the LOS velocity field the long-wavelength signal due to the interseismic strain assuming that the regional deformation due to the secular loading arises from buried displacement below the NAF. To model this secular loading, we use the far field (>20 km away from the fault) LOS velocity field data (with the Orta earthquake region being masked). We invert for a right-lateral sense of slip on a single fault patch buried below 10 km to infinity (900 km) and obtain ∼25 mm/yr of interseismic slip rate. However, the model does not entirely account for the long-wavelength signal in the velocity field, implying the presence of unwrapping and unmodeled atmospheric errors, and orbital residuals in the data. We therefore obtain a variable interseismic slip model using multiple fault patches (12 triangles) to flatten the far field velocity field required for modeling the distribution of shallow creep on the fault (Figure S2, supporting information). We subtract this inverted interseismic model from the LOS velocity field and obtain a residual LOS velocity field that is considered as a creep signal in vicinity of the fault (Figure 8). The residual LOS velocities show a sharp color contrast across the fault that can also be seen in the profiles shown in Figure 8b. Some of the remaining velocities, which are on the corner of the tracks with ±2–3 mm/yr, in the velocity field are, however, most probably due to atmospheric artifacts or unmodeled orbital errors but these do not affect offset at fault. In addition, the postseismic surface deformation associated with the 2000 Orta earthquake [*Cakir and Akoglu*, 2008] becomes more prominent and appears as circular area of range decrease ∼30 km across anomaly with a blue color.

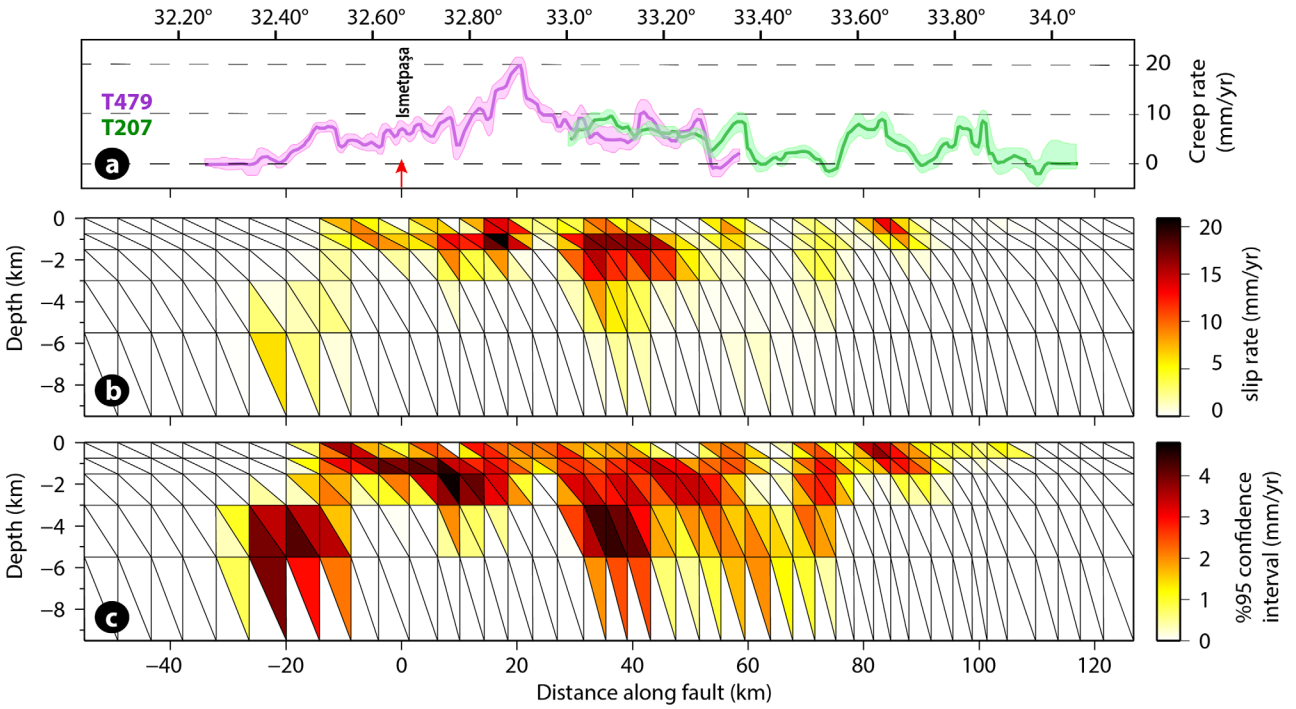


**Figure 9.** (a) Variation of surface creep rate along the fault; (b) depth distribution of the variable aseismic slip on the Ismetpaşa creeping segment. Red arrow indicates the position of the geodetic network located 3.5 km east of the train station near Hamamlı village at Ismetpaşa. Slip is heterogeneously distributed along the fault and confined mostly to uppermost 5 km of the seismogenic crust with a maximum slip of ∼20 ± 2 mm/yr 20 km west of Ismetpaşa. (c) Uncertainty of the slip distribution with depth obtained from inversions of 200 InSAR data sets perturbed with synthetic noise.

To model the creep on the fault surface, we formed a vertical fault from surface to a depth of 10 km, using quadrangles of about 5 km long along the fault strike. The width of the quadrangles increases from 1 to 3 km in the downdip direction (Figures 8 and 9). To evaluate the uncertainty of slip distribution, we first estimate a 1-D covariance function for each data set by radially averaging a 2-D autocorrelation function calculated using the power spectrum of the data in the far field where there are no orbital ramps or deformation signal due to aseismic creep [*Hanssen*, 2001]. We then fit a colored noise model [*Lennon*, 2000] to the 1-D covariance function. Using the procedures in *Fukushima et al*. [2003], for each data set on the two tracks we construct 200 simulations of spatially correlated random noise that matches the colored noise model. We use them to perturb each of our original data sets [*Funning et al*., 2005] which are then inverted for pure right-lateral strike slip (locked on the fault edges, except at its top) using a scale-dependent umbrella-smoothing operator to avoid any unphysical oscillatory slip distribution. A smoothing factor of 0.5 is used since lower values predict slip rates much higher than the interseismic slip rates estimated from the GPS measurements (24.2 ± 0.2 mm/yr) by *Reilinger et al*. [2006] and from InSAR (25 ± 1.5 mm/yr) in this study. After calculating the mean slip, we estimate %95 confidence intervals from its distribution on each triangular patch. The results show a shallow creeping depth (mostly above 5 km) and an intermittent slip distribution with a highest rate of 20 ± 2 mm/yr on several patches along the fault, similar to that inferred along the Hayward fault [*Schmidt et al*., 2005] (Figure 9). Although the surface creep deduced from offsets of best fitting lines correlates to some extent with the creep inferred with Poly3Dinv modeling at depth, the largest patch located ∼40 km east of Ismetpaşa is not obvious in the surface creep rate curves. Figure 8b illustrates that the model explains the LOS data reasonably well (∼1.25 mm/yr RMS; Figure S3, supporting information). As expected, checker-box tests show that slip resolution decreases with increasing depth, but as shown in Figure S4 (supporting information) the InSAR data have an adequate resolution in constraining the shallow slip (<5 km) on the fault.

## 4. Discussion

The mechanical behavior of active fault zones can vary from continuous aseismic creep to sudden rupture during earthquakes, and the same fault zone may evolve either laterally or at depth from seismic to

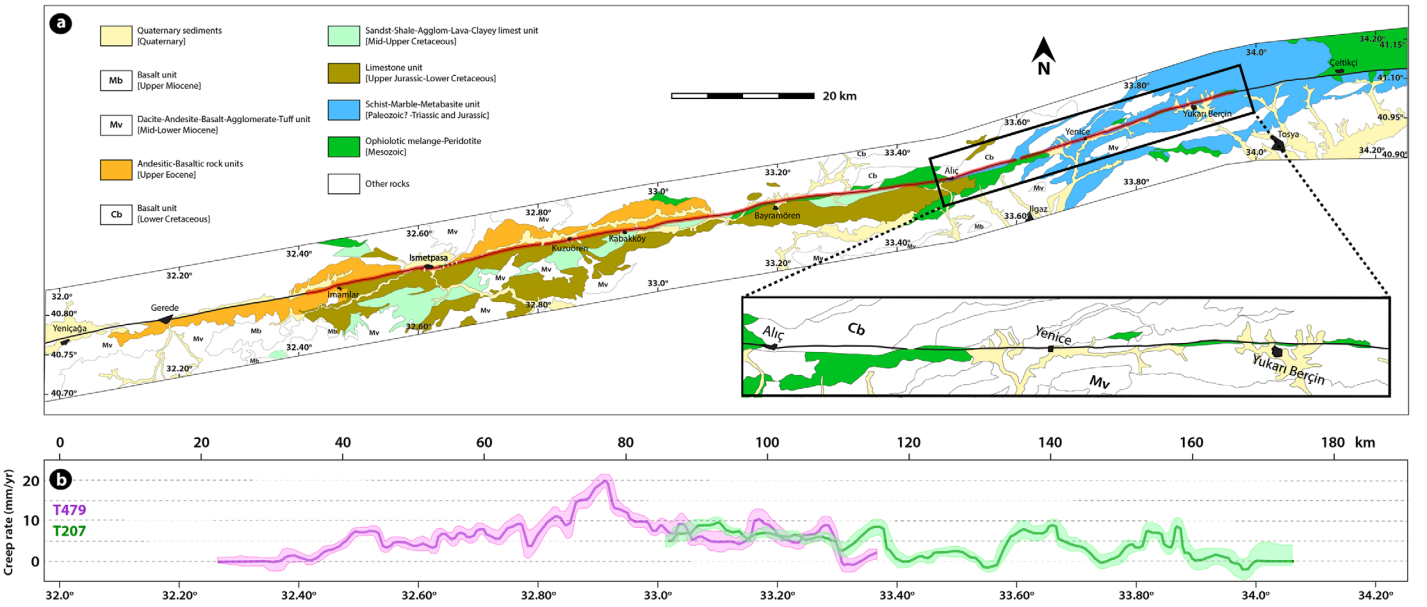


**Figure 10.** (a) Geology map of the study region simplified from *Herece and Akay* [2003] with surface creep rates along the North Anatolian Fault obtained in this study. Geological units presumably involved in creeping are shown in colors and the others are labeled in white with abbreviations. Black and red lines represent the active fault and the creeping segment, respectively. The eastern end of the creeping section can be clearly seen in the inset rectangle. (b) Creep rates and error ranges for two individual tracks are indicated in purple and green colors as in Figure 6.

aseismic deformation [*Freed*, 2007; *Gratier et al*., 2013]. It is therefore important to determine whether this transition is geologically and tectonically controlled since some types of rocks are more prone to seismic failure while the others are more likely to exhibit aseismic creep [*Gratier et al*., 2013]. If the fault zone rocks are weaker than the surrounding rocks and do not heal after the rupture, they may exhibit stable sliding friction behavior, so called velocity-strengthening conditions [*Carpenter et al*., 2011]. Inherited tectonic structures, the presence of weak rocks or the thickness of the gouge zone may control the distribution of surface creep. Serpentines [*Allen*, 1968] and clay rich lithology [*Warr and Cox*, 2001] have long been identified as zones of structural characteristics with phyllosilicate foliations resulting into fault weakening [*Collettini et al*., 2009]. Similarly, calcareous rocks with phyllosilicates are able to creep in the upper crust by pressure solution [*Gratier et al*., 2013].

Analysis of geological maps reveals that the aseismic surface creep can be, to some extent, correlated with the geology along the North Anatolian Fault (Figure 10). The major surface creep in the shallow depths of the western part of the creeping segment, overlapping with 1944 earthquake rupture is correlated with the Upper Jurassic-Lower Cretaceous limestone unit, probably due to pressure solution. In the eastern part of the creeping segment, which overlaps with the 1943 earthquake rupture, aseismic slip is possibly related to the serpentinite bodies marked in the geology map as Mesozoic ophiolotic mélange along the fault zone (Figure 10a). There appears to be no correlation, however, between the variation of creep rate and surface lithology along the fault (Figure 10).

The downward circulation of meteoric fluids may also contribute to the creep in the weaker upper crust as shown by the numerous hot springs along the Alpine active fault zone in New Zealand [*Allis and Shi*, 1995], and in particular in the western and central western segments of the North Anatolian Fault zone. In fact, Paleozoic metamorphic rocks, along with Mesozoic limestone and flysch, comprise the basement rocks in the geothermal fields along the North Anatolian Fault zone [*Erisen et al*., 1996]. Therefore, both the geology and the downward circulation of meteoric fluids might have a control on the aseismic slip of the Ismetpaşa segment.

Although it is not known whether or not the fault was creeping before the 1944 earthquake, postseismic measurements at Ismetpaşa reveals an exponential decay in creep rate that appears to have graded into a steady state slip over the last decades or so (Figure 11). This suggests that aseismic slip may continue for decades, and plausibly during the entire earthquake cycle (∼200–300 years). Change in the creep rate with

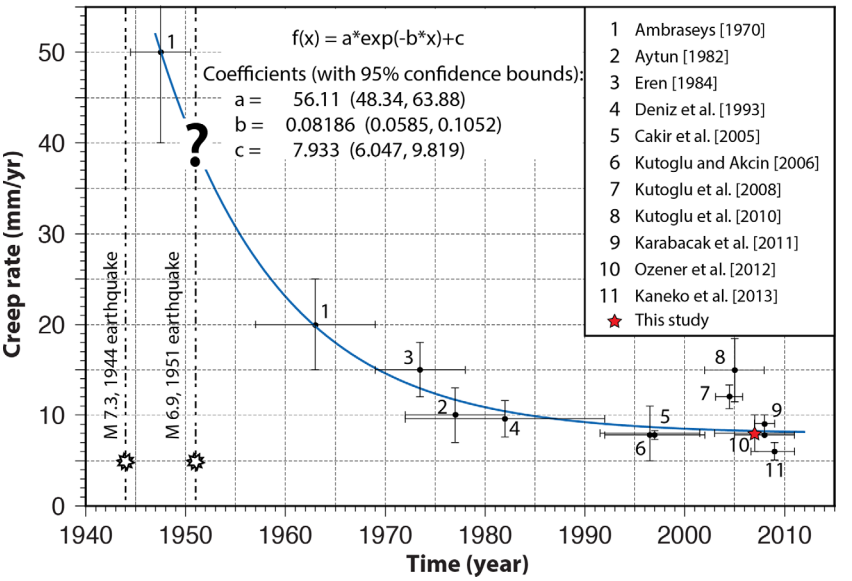


**Figure 11.** Time history of surface creep at Ismetpaşa as reported by various studies following the 1944 earthquake [after *Cakir et al.*, 2005]. Horizontal and vertical bars are the time window and error range of measurements, respectively. The question mark corresponds to the unknown effect of the 1951 earthquake on creep rate. Curve shows the fit of the exponential relaxation function to the change of the creep rate with time [*Savage et al.*, 2005].

time is fitted to an exponential relaxation function that suggests Newtonian behavior of creep in a ductile shear zone [*Savage et al.*, 2005]. Using fully dynamic models of earthquake cycles, *Kaneko et al.* [2013] inferred that the friction behavior of Ismetpaşa creeping segment is velocity strengthening at shallow depths, changing to velocity weakening at 3–6 km depth. Our models suggest that these properties may vary in space along the fault.

## 5. Conclusions

We have studied the spatial distribution of aseismic creep on the Ismetpaşa segment of the NAF using Envisat ASAR data between 2003 and 2010. The surface velocity field obtained with the PSI technique provides a tighter constraint on the characteristics of surface creep compared to conventional InSAR techniques. The results reveal a surface creep rate of $8 \pm 2$ mm/yr at Ismetpaşa which reaches a maximum of $20 \pm 2$ mm/yr 20 km to the east. Aseismic slip releases every year a moment of $6.2 \times 10^{16}$ Nm, which is equivalent of an earthquake of Mw = 5.1. It implies that a significant portion of the fault is locked and accumulates interseismic strain to be released coseismically as demonstrated with the 1943, 1944, and 1951 earthquakes. High creep rates coincide mostly with the 1951 and eastern part of the 1944 earthquake ruptures. Measurements over the last 60 years show that creep on the Ismetpaşa segment has graded with time into a steady state rate after the 1944 and/or 1951 earthquakes (Figure 11), suggesting that it was probably triggered as postseismic afterslip following the 1944 earthquake as was found with the surface deformation following the 1999 Izmit earthquake [*Cakir et al.*, 2012].

Three-dimensional elastic dislocation modeling suggests that surface creep occurs along a 100 km long section since the easternmost 20 km creeping section estimated with best fitting linear approximations (Figure 6b) is not detected with the 3-D elastic dislocation modeling (Figure 9) probably due to high level of noise in this section. The creeping section extends at least 30 km further east compared to the previous studies [*Cakir et al.*, 2005; *Kaneko et al.*, 2013]. Modeling results indicate a shallow creeping depth, mostly less than 5 km, in good agreement with the velocity-strengthening at shallow depths deduced from dynamic models by *Kaneko et al.* [2013] and elastic dislocation models by *Cakir et al.* [2005]. Thus, the Ismetpaşa segment appears to be locked with a higher stressing rate at the lower seismogenic crust, which is able to generate strain release during moderate-large earthquakes such as those that occurred in the 1943, 1944, and 1951

earthquakes. An analysis of the geological structures suggests that aseismic slip along the Ismetpaşa creeping segment is mainly controlled by the limestone and serpentine bodies.

**Acknowledgments**
InSAR data were copyrighted and obtained through the category-1 project AOTR-2436 of the European Space Agency and the Geohazard Supersites program. SAR images were processed at the TUBITAK ULAKBIM High Performance and Grid Computing Centre of Turkey. Financial support is from TUBITAK project 107Y281. This is part of the dissertation of Esra Cetin who is supported by the French Embassy (in Turkey) Bourse Etudes scholarship program (778343D and 797216D) and by the TUBITAK-BIDEB 2214B scholarship program during the completion of this work. Most of the figures in this paper were generated using the public domain Generic Mapping Tools (GMT) software [*Wessel and Smith*, 1998]. We thank Tim Wright and anonymous reviewer for constructive comments that greatly improved this manuscript.

## References

Allen, C. R. (1968), The tectonic environments of seismically active and inactive areas along the San Andreas fault system, *Stanford Univ. Publ. Geol. Sci.*, *11*, 70–80.
Allis, R. G., and Y. Shi (1995), New insights to temperature and pressure beneath the central Southern Alps, New Zealand, *N. Z. J. Geol. Geophys.*, *38*, 585–592.
Ambraseys, N. N. (1970), Some characteristic features of the Anatolian fault zone, *Tectonophysics*, *9*, 143–165.
Aytun, A. (1982), Creep measurements in the Ismetpaşa region of the North Anatolian Fault Zone, in *Multidisciplinary Approach to Earthquake Prediction*, edited by A. M. Isikara and A. Vogel, vol. 2, pp. 279–292, Friedr. Vieweg & Sohn, Braunschweig, Germany.
Barka, A. A. (1996), Slip distribution along the North Anatolian fault associated with the large earthquakes of the period 1939–1967, *Bull. Seismol. Soc. Am.*, *86*, 1238–1254.
Barka, A. A., and K. Kadinsky-Cade (1988), Strike-slip fault geometry in Turkey and its influence on earthquake activity, *Tectonics*, *7*(3), 663–684.
Bilham, R. (1989), Surface slip subsequent to the 24 November 1987 Superstition Hills, California, earthquake monitored by digital creepmeters, *Bull. Seismol. Soc. Am.*, *79*, 424–450.
Burford, R. O., and P. W. Harsh (1980), Slip on the San Andreas fault in central California from alignment array surveys, *Bull. Seismol. Soc. Am.*, *70*, 1223–1261.
Bürgmann, R., D. Schmidt, R. Nadeau, M. d'Alessio, E. Fielding, D. Manaker, T. McEvilly, and M. H. Murray (2000), Earthquake potential along the northern Hayward fault, *Science*, *289*, 1178–1182.
Cakir, Z., and A. M. Akoglu (2008), Synthetic aperture radar interferometry observations of the M = 6.0 Orta earthquake of 6 June 2000 (NW Turkey): Reactivation of a listric fault, *Geochem. Geophys. Geosyst.*, *9*, Q08009, doi:10.1029/2008GC002031.
Cakir, Z., A. M. Akoglu, S. Belabbes, S. Ergintav, and M. Meghraoui (2005), Creeping along the Ismetpaşa section of the North Anatolian Fault (Western Turkey): Rate and extent from InSAR, *Earth Planet. Sci. Lett.*, *238*, 225–234.
Cakir, Z., S. Ergintav, H. Ozener, U. Dogan, A. M. Akoglu, M. Meghraoui, and R. Reilinger (2012), Onset of aseismic creep on major strike-slip faults, *Geology*, *40*(12), 1115–1118.
Carpenter, B. M., C. Marone, and D. M. Saffer (2011), Weakness of the San Andreas Fault revealed by samples from the active fault zone, *Nat. Geosci.*, *4*, 251–254.
Champenois, J., B. Fruneau, E. Pathier, B. Deffontaines, K.-C. Lin, and J.-C. Hu (2012), Monitoring of active tectonic deformations in the Longitudinal Valley (Eastern Taiwan) using Persistent Scatterer InSAR method with ALOS PALSAR data, *Earth Planet. Sci. Lett.*, *337–338*, 144–155.
Cigna, F., B. Osmanoglu, E. Cabral-Cano, T. H. Dixon, J. A. Avila-Olivera, V. H. Garduno-Monroy, C. DeMets, and S. Wdowinski (2011), Monitoring land subsidence and its induced geological hazard with synthetic aperture radar interferometry: A case study in Morelia, Mexico, *Remote Sens. Environ.*, *117*, 146–161.
Collettini, C., A. Niemeijer, C. Viti, and C. Marone (2009), Fault zone fabric and fault weakness, *Nature*, *462*, 907–910.
Dehghani, M., A. Hooper, R. Hanssen, M. J. V. Zoej, S. Saatchi, and I. Entezam (2013), Hybrid conventional and persistent scatterer SAR interferometry for land subsidence monitoring in Tehran Basin, Iran, *ISPRS J. Photogramm. Remote Sens.*, *79*, 157–170.
Deniz, R., A. Aksoy, D. Yalin, H. Seeger, and O. Hirsch (1993), Determination of crustal movement in Turkey by terrestrial geodetic methods, *J. Geodyn.*, *18*, 13–22.
Eren, K. (1984), Strain analysis along the North Anatolian fault by using geodetic surveys, *Bull. Geod.*, *58*, 137–149.
Erisen, B., I. Akkus, N. Uygur, and A. Kocak (1996), *Türkiye Jeotermal Envanteri*, Gen. Dir. of Miner. Res. and Explor., Ankara.
Farr, T. G., et al. (2007), The shuttle radar topography mission, *Rev. Geophys.*, *45*, RG2004, doi:10.1029/2005RG000183.
Ferretti, A., C. Prati, and F. Rocca (2000), Nonlinear subsidence rate estimation using permanent scatterers in differential SAR interferometry, *IEEE Trans. Geosci. Remote Sens.*, *38*, 2202–2212.
Ferretti, A., C. Prati, and F. Rocca (2001), Permanent scatterers in SAR interferometry, *IEEE Trans. Geosci. Remote Sens.*, *39*, 8–20.
Freed, A. M. (2007), Afterslip (and only afterslip) following the 2004 Parkfield, California, earthquake, *Geophys. Res. Lett.*, *34*, L06312, doi:10.1029/2006GL029155.
Fukushima, Y., O. Nishizawa, H. Sato, and M. Ohtake (2003), Laboratory study on scattering characteristics in rock samples, *Bull. Seismol. Soc. Am.*, *93*, 253–263.
Funning, G. J., B. Parsons, and T. J. Wright (2005), Surface displacements and source parameters of the 2003 Bam (Iran) earthquake from Envisat advanced synthetic aperture radar imagery, *J. Geophys. Res.*, *110*, B09406, doi:10.1029/2004JB003338.
Gratier, J.-P., F. Thouvenot, L. Jenatton, A. Tourette, M.-L. Doan, and F. Renard (2013), Geological control of the partitioning between seismic and aseismic sliding behaviours in active faults: Evidence from the Western Alps, France, *Tectonophysics*, *600*, 226–242.
Hanssen, R. F. (2001), *Radar Interferometry: Data Interpretation and Error Analysis*, vol. 2, Springer, N. Y.
Herece, E., and E. Akay (2003), *Atlas of North Anatolian Fault, Spec. Publ. Ser. 2*, Gen. Dir. of Miner. Res. and Explor., Ankara.
Hooper, A. (2008), A multi-temporal InSAR method incorporating both persistent scatterer and small baseline approaches, *Geophys. Res. Lett.*, *35*, L16302, doi:10.1029/2008GL034654.
Hooper, A., H. Zebker, P. Segall, and B. Kampes (2004), A new method for measuring deformation on volcanoes and other natural terrains using InSAR persistent scatterers, *Geophys. Res. Lett.*, *31*, L23611, doi:10.1029/2004GL021737.
Hooper, A., P. Segall, and A. Zebker (2007), Persistent scatterer interferometric synthetic aperture radar for crustal deformation analysis, with application to Volcan Alcedo, Galapagos, *J. Geophys. Res.*, *112*, B07407, doi:10.1029/2006JB004763.
Kampes, B. M. (2005), *Displacement Parameter Estimation Using Permanent Scatterer Interferometry*, Ph.D. thesis, Delft Univ. of Technol., Delft, Netherlands.
Kampes, B. M., and S. Usai (1999), Doris: The delft object-oriented radar interferometric software, paper presented at ITC 2nd ORS Symposium, Int. Inst. for Geoinf. Sci. and Earth Obs., Enchede, Netherlands.
Kaneko, Y., Y. Fialko, D. T. Sandwell, X. Tong, and M. Furuya (2013), Interseismic deformation and creep along the central section of the North Anatolian fault (Turkey): InSAR observations and implications for rate-and-state friction properties, *J. Geophys. Res.*, *118*, 316–331, doi:10.1029/2012JB009661.
Karabacak, V., E. Altunel, and Z. Cakir (2011), Monitoring aseismic creep along the North Anatolian Fault (Turkey) using ground-based LIDAR, *Earth Planet. Sci. Lett.*, *304*, 64–70.

Ketelaar, K. (2008), Satellite radar interferometry, subsidence monitoring techniques, PhD thesis, Delft Univ. of Technol. Delft, Netherlands.
Kutoglu, H. S., and H. Akcin (2006), Determination of 30-year Creep on the Ismetpaşa segment of the North Anatolian Fault using an old geodetic network, *Earth Planets Space*, *58*, 937–942.
Kutoglu, H. S., H. Akcin, H. Kemaldere, and K. S. Gormus (2008), Triggered creep rate on the Ismetpasa segment of the North Anatolian Fault, *Nat. Hazards Earth Syst. Sci.*, *8*, 1369–1373.
Kutoglu, H. S., H. Akcin, O. Gundogdu, K. S. Gormus, and E. Koksal (2010), Relaxation on the Ismetpasa segment of the North Anatolian Fault after Golcuk Mw = 7.4 and Duzce Mw = 7.2 shocks, *Nat. Hazards Earth Syst. Sci.*, *10*, 2653–2657.
Lennon, J. J. (2000), Red-shifts and red herrings in geographical ecology, *Ecography*, *23*, 101–113.
Maerten, F., P. Resor, D. Pollard, and L. Maerten (2005), Inverting for slip on three dimensional fault surfaces using angular dislocations, *Bull. Seismol. Soc. Am.*, *95*(5), 1654–1665.
Motagh, M., J. Hoffmann, B. Kampes, M. Baes, and J. Zschau (2007), Strain accumulation across the Gazikoy-Saros segment of the North Anatolian Fault inferred from persistent scatterer interferometry and GPS measurements, *Earth Planet. Sci. Lett.*, *255*, 432–444.
Ozener, H., A. Dogru, and B. Turgut (2012), Quantifying aseismic creep on the Ismetpaşa segment of the North Anatolian Fault Zone (Turkey) by 6 years of GPS observations, *J. Geodyn.*, *67*(7), 72–77.
Peyret, M., S. Dominguez, R. Cattin, J. Champenois, M. Leroy, and A. Zajac (2011), Present-day interseismic surface deformation along the Longitudinal Valley, eastern Taiwan, from a PS-InSAR analysis of the ERS satellite archives, *J. Geophys. Res.*, *116*, B03402, doi:10.1029/2010JB007898.
Reilinger, R. E., et al. (2006), GPS constraints on continental deformation in the Africa-Arabia-Eurasia continental collision zone and implications for the dynamics of plate interactions, *J. Geophys. Res.*, *111*, B05411, doi:10.1029/2005JB004051.
Rosen, P., S. Hensly, G. Peltzer, and M. Simons (2004), Updated repeat orbit interferometry package released, *Eos Trans. AGU*, *85*(5), 47.
Şaroğlu, F., Ö. Emre, and I. Kuşçu (1992), *Active Fault Map of Turkey*, Gen. Dir. of Miner. Res. and Explor., Ankara.
Savage, J. C., and R. O. Burford (1973), Geodetic determination of relative plate motion in central California, *J. Geophys. Res.*, *78*, 832–845.
Savage, J. C., and M. Lisowski (1993), Inferred depth of creep on the Hayward fault, central California, *J. Geophys. Res.*, *98*, 787–793.
Savage, J. C., J. L. Svarc, and S.-B. Yu (2005), Postseismic relaxation and transient creep, *J. Geophys. Res.*, *110*, B11402, doi:10.1029/2005JB003687.
Schmidt, D. A., R. Bürgmann, R. M. Nadeau, and M. A. d'Alessio (2005), Distribution of aseismic slip-rate on the Hayward fault inferred from seismic and geodetic data, *J. Geophys. Res.*, *110*, B08406, doi:10.1029/2004JB003397.
Stein, R. S., A. Barka, and J. H. Dieterich (1997), Progressive failure on the North Anatolian fault since 1939 by earthquake stress triggering, *Geophys. J. Int.*, *128*, 594–604.
Taymaz, T., T. J. Wright, S. Yolsal, O. Tan, E. Fielding, and G. Seyitoglu (2007), Source characteristics of the 6 June 2000 Orta, Cankiri (central Turkey) earthquake: A synthesis of seismological, geological and geodetic (InSAR) observations, and internal deformation of the Anatolian plate, *Geol. Soc. Spec. Publ.*, *291*, 259–290.
Thatcher, W. (1979), Systematic inversion of geodetic data in central California, *J. Geophys. Res.*, *84*, 2283–2297.
Thomas, M. Y., J. P. Avouac, J. Champenois, J. C. Lee, and L. C. Kuo (2014), Spatio-temporal evolution of seismic and aseismic slip on the Longitudinal Valley Fault, Taiwan, *J. Geophys. Res.*, *119*, doi:10.1002/2013JB010603, in press.
Warr, L. N., and S. Cox (2001), Clay mineral transformations and weakening mechanisms along the Alpine fault, New Zealand, *Geol. Soc. Spec. Publ.*, *186*, 85–101.
Wei, M., D. Sandwell, and Y. Fialko (2009), A silent M4.8 event of October 3-6, 2006, on the Superstition Hills Fault, Southern California, *J. Geophys. Res.*, *114*, B07402, doi:10.1029/2008JB006135.
Wessel, P., and W. H. F. Smith (1998), New improved version of Generic Mapping Tools released, *Eos Trans. AGU*, *79*(47), 579.